Indian Journal of Biochemistry & Biophysics
Vol. 63, February 2026, pp. 163-180
DOI: 10.56042/ijbb.v63i2.19854

In vitro anti-mitotic activity of *Hibiscus rosa-sinensis* extract: Network pharmacology, Molecular docking, MM/GBSA dynamic simulation, and DFT calculation

Thapa S[1], Arora M[2], Mahmood AAR[3], Biradar MS[4]*, Aleesha MS[4] & Maurya SN[5]

[1]Department of Pharmaceutical Chemistry, East Point College of Pharmacy, Bengaluru-560 043, Karnataka, India

[2]Faculty of Health Sciences, Villa College, QI Campus, Rah Dhebai Hingun, Malé-20373, Republic of Maldives

[3]Department of Pharmaceutical Chemistry, College of Pharmacy, University of Baghdad, Bab-Al-Mouadam, Baghdad-10001, Iraq

[4]Department of Pharmaceutical Chemistry, Al-Ameen College of Pharmacy, Bengaluru-560 027, Karnataka, India

[5]Department of Pharmacy, Universal College of Medical Sciences, Bhairahawa-32900, Nepal

Received 19 May 2025; *revised 24 May 2025*

The limitations and adverse effects of current chemotherapeutic drugs make the search for novel, plant-derived anticancer agents a global priority. Despite its widespread application in traditional medicine, *Hibiscus rosa-sinensis* has not been extensively studied for anti-mitotic activity as a key cancer inhibitor. This integrated study included *in vitro* tests and computational modeling to evaluate *Hibiscus rosa-sinensis* extract's anti-mitotic activity. *in vitro* results showed a dose-dependent reduction of root development (up to 76.3%) and a significant drop in mitotic index (16.2% to 2.6%) at 400 µg/mL. Seven bioactive compounds identified by phytochemical screening have been examined using network pharmacology to determine their interaction with mitosis-regulating targets, including cancer cell proliferation-associated EGFR and AKT1 proteins. Quercetin-3,7-diglucoside bound strongly to EGFR (-9.6 kcal/mol) and AKT1 (-11.0 kcal/mol) in molecular docking, which was supported by free energy calculations and molecular dynamics simulations as stable interactions. DFT study confirmed the compound's electronic stability and reactivity. These findings suggest *Hibiscus rosa-sinensis* may be a promising anti-mitotic agent and worth further study for cancer therapy.

Keywords: Anti-cancer, AKT1 signaling, Bioinformatics integration, EGFR inhibition, *In silico* studies, Natural product

Global health is increasingly affected by cancer, the major cause of illness and mortality. According to the IARC, 20 million new cancer cases and 9.7 million cancer-related deaths occurred worldwide in 2022. Over 35 million more cancer cases are expected by 2050, a 77% increase from 2022 predictions[1,2]. This rise is due to aging populations, lifestyle changes, and environmental risk factors. Tumorigenesis involves abnormal mitosis and unregulated cell division. Targeting mitotic pathways has been useful in cancer treatment, however side effects and drug resistance limit the efficacy of current anti-mitotic treatments. The cell cycle, including mitosis, controls cell division[3]. Cancer-causing mitotic disruptions cause uncontrolled cell proliferation. Thus, discovering organic compounds that modulate mitotic processes is interesting for cancer treatment[4,5].

Medicinal plants have long provided therapeutic compounds, including anti-cancer medications. The tropical plant hibiscus, commonly referred to as hibiscus, is utilized in traditional Chinese medicine (TCM) for its anti-inflammatory, antioxidant, cooling, and detoxifying effects[6,7]. Its flavonoids, alkaloids, and phenolic acids are of interest due to their potential health benefits[8]. Quercetin-3-diglucoside, cyanidin-3-sophoroside-5-glucoside, rutin, campesterol, stigmasterol, kaempferol-3-xylosylglucoside, myricetin, and cyanidin-3, 5-, and 3, 7-diglucoside are abundant in the flowers[9]. These phytoconstituents produced the plant's varied pharmacological effects. The plant modulates biological processes, including cellular development and death, according to several studies[10]. Hibiscus has been studied as a means of treating cancer. K. Goldberg *et al*. showed that aqueous *Hibiscus rosa-sinensis* flower extract suppressed cancer cell growth in a concentration-dependent manner without affecting non-transformed cell proliferation[11]. The Hibiscus family has strong anticancer properties. This plant was chosen for our research.

*Correspondence:
E-mail: mahalakshmisb12@gmail.com
Suppl. data available on the respective page of NOPR

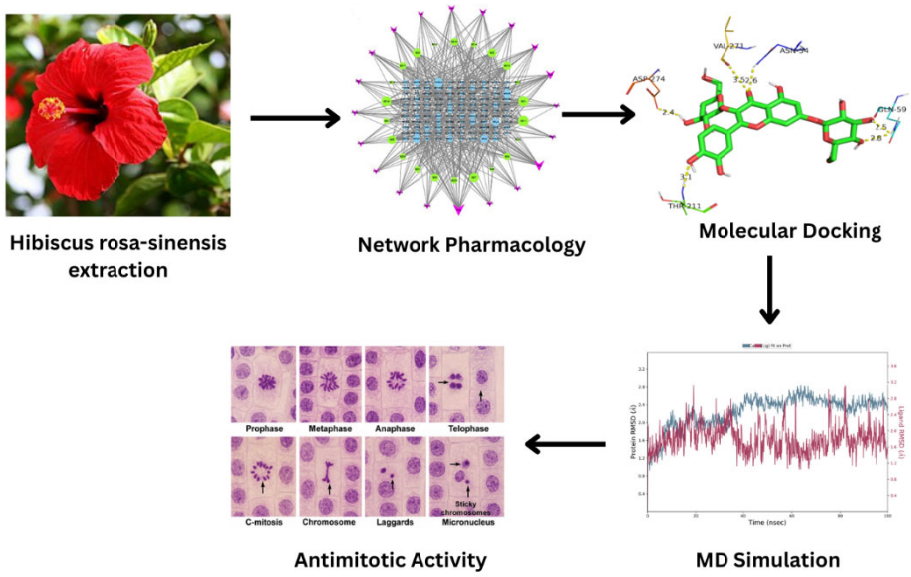

Graphical abstract

This study combines network pharmacology, molecular docking, molecular mechanics/generalized born surface area (MM/GBSA) dynamic simulation, and density functional theory (DFT) calculations to evaluate *Hibiscus rosa-sinensis* extract's *in vitro* anti-mitotic efficacy. Network pharmacology examines plant bioactive substances and mitosis-related biological targets[12]. Molecular docking, MM/GBSA simulations, and DFT calculations will provide insight into the protein-ligand interactions that control its anti-mitotic activities and their electronic properties and stability[13–15]. This research will combine computational methods with experimental validation to better understand *Hibiscus rosa-sinensis*' anti-mitotic ability and promise as a cancer treatment.

Materials and Methods

Authentication of plant

From Nawalparasi district, Nepal, fresh *Hibiscus rosa-sinensis* flowers were collected. Department of Horticulture and Plant Protection, Institute of Agriculture and Animal Sciences (IAAS), Ranigaon, Bhairahawa, Rupandehi, Nepal, validated the herbarium.

Preparation and extraction

The shade-dried samples were milled into a coarse powder using a mechanical grinder and sieved through sieve no. 25 for uniformity. The hot extraction was performed via a Soxhlet apparatus, in which 100 g of powdered flowers were mixed with 500 mL of 95% ethanol in a round-bottom flask. The ethanol is safe to use and has no adverse effects. The extraction cycle was performed at 60±2°C for 6 h, with two-five cycles ensuring complete extraction. The plant extract was evaporated at room temperature (25± 2°C) for 2 days. The concentrated extract was then dried in a vacuum desiccator to remove residual solvent and stored at 4°Cin amber-colored vials until further use.Equation A1 was used to calculate the extract yield percentage[16].

$$\%\,Yield = \frac{\text{weight of extract}}{weight\ of\ powder\ taken} x\ 100\% \ldots\ (A1)$$

Preliminary phytochemical screening

Traditional qualitative phytochemical screening was used to identify key phytoconstituent classes in *Hibiscus rosa-sinensis*' dried ethanolic extract. Shinoda and alkaline reagent tests confirmed flavonoids; Mayer, Wagner, and Dragendorff identified alkaloids. The ferric chloride test found phenols and tannins, whereas continual froth development indicated saponins. While Keller-Kiliani identified glycosides, Salkowski and Liebermann-Burchard detected terpenoids and steroids. The tests demonstrated the extract's diverse secondary metabolites, suggesting biological activity.

Network pharmacology

Preliminary phytochemical screening

The prepared extracts were analyzed for alkaloids, glycosides, tannins, phenolic compounds, carbohydrates, terpenoids, and flavonoids. The constituents of the flower extract were confirmed using established protocols[17].

Phytochemical identification and target prediction

In our previous study, we identified seven phytoconstituents from *Hibiscus rosa-sinensis* flower extract through LC-MS analysis[18]. We have taken all seven phytoconstituents in this study for the network. The selected phytoconstituents include nicotinic acid, quercetin-3,7-diglucoside, kaempferol-3-xylosylglucoside, quercetin-3-sophorotrioside, quercetin, cyanine, and β-Sitosterol. Seven bioactive compounds from *Hibiscus rosa-sinensis* were validated using phytochemical databases, including IMPPAT 2.0 and PubChem. Canonical SMILES were retrieved and input into Swiss Target Prediction (http://www.swisstargetprediction.ch/) to predict probable protein targets based on structural similarity and bioactivity data.

Disease-related gene collection

Oral cancer-associated genes were obtained from the GeneCards (https://www.genecards.org/) databases using "antimitotic gene" as the search keyword. Duplicates were removed, and intersecting targets between predicted compound targets and disease-related genes were identified using the InteractiVenn tool (https://www.interactivenn.net/)[19].

PPI network construction and hub gene identification

The overlapping targets were uploaded to the STRING database v11.5 (https://string-db.org/) to generate a protein–protein interaction (PPI) network with a confidence score cutoff of 0.7[20]. The resulting network was visualized using Cytoscape v3.10.2. Key nodes were identified using the CytoHubba plugin, ranking by maximal clique centrality (MCC), degree, and closeness metrics[21].

Functional and pathway enrichment analysis

Gene Ontology (GO) and KEGG pathway enrichment analyses were conducted via the Shiny GO 0.82 web browser (https://bioinformatics.sdstate.edu/go/), setting the threshold at FDR < 0.05. Categories included biological process, cellular component, and molecular function. Enrichment data were visualized as bar plots and hierarchical clustering trees using ShinyGO 0.82[22].

Molecular docking analysis

Software and Database: AutoDock Tools 1.5.7 (http://vina.scripps.edu/), AutoDock v1.2.0, OpenBabel 2.4.1 software, BIOVIA Discovery Studio Visualizer 2021 (https://discover.3ds.com/discovery-studio-visualizer-download), RCSB Protein Data Bank (https://www.rcsb.org/).

The structure of active phytoconstituents was retrieved in 3D sdf format from PubChem. The phytoconstituents were converted from sdf to pdbqt format with Openbabel. Openbabel is a free tool that allows to convert one file type to another. This makes the task easier for the subsequent docking operation[23]. The energy was minimized using MMFF94 force fields. The EGFR protein and AKT1 play critical roles in cell signalling pathways that control proliferation, survival, differentiation, and migration. EGFR is activated after binding to a particular ligand, resulting in dimerization and autophosphorylation, which initiate downstream cascades. AKT1 is activated downstream of PI3K. The activation of PI3K causes the membrane to produce PIP3. AKT1 binds to PIP3 via its PH domain and then translocated to the membrane. This enhances cell survival and increases glucose metabolism[24].

Each target was assigned a protein, and the EGFR protein PDBID 1M17[25] and the AKT1 protein PDBID 4EJN[26] were chosen. The 1M17 and 4EJN with a x-ray resolution of 2.60 Å and 2.19 Å, respectively, were retrieved from the RCSB protein data bank (https://www.rcsb.org/).Both proteins were mutation-free and contained a co-crystal ligand. The proteins were validated by Ramachandran plot analysis. For both proteins, above 92% amino acids were present in the allowed region (Fig. 1a & b). These proteins were prepared for docking by removing water molecules and adding hydrogen bonds and Kollman charges with the AutoDock Vin Tool v1.5.7. The prepared proteins were stored in the pdbqt format[27]. A grid box was generated around the active site (co-crystal ligand), and its properties were recorded in a CSV file (Table 1). The active sites for both proteins are listed below (Table 1). The docking operation was conducted with the command platform in Dell Vastro 14 3000 series windows operating system. This facilitates the docking of more than 100 ligands at once, utilizing AutoDock Vina v1.2.0. This saves time and is simple to use if the ligand, protein, and other files are in the correct file format. Furthermore, we chose the gradient optimization approach because, in comparison to other approaches, it provides AutoDock Vina with faster convergence, greater sampling efficiency, better repeatability, easier handling of big ligands, and cheaper computational cost. AutoDock Vina globally optimizes initially placed binding conformations, sampling potential ligand-binding conformations and predicting the

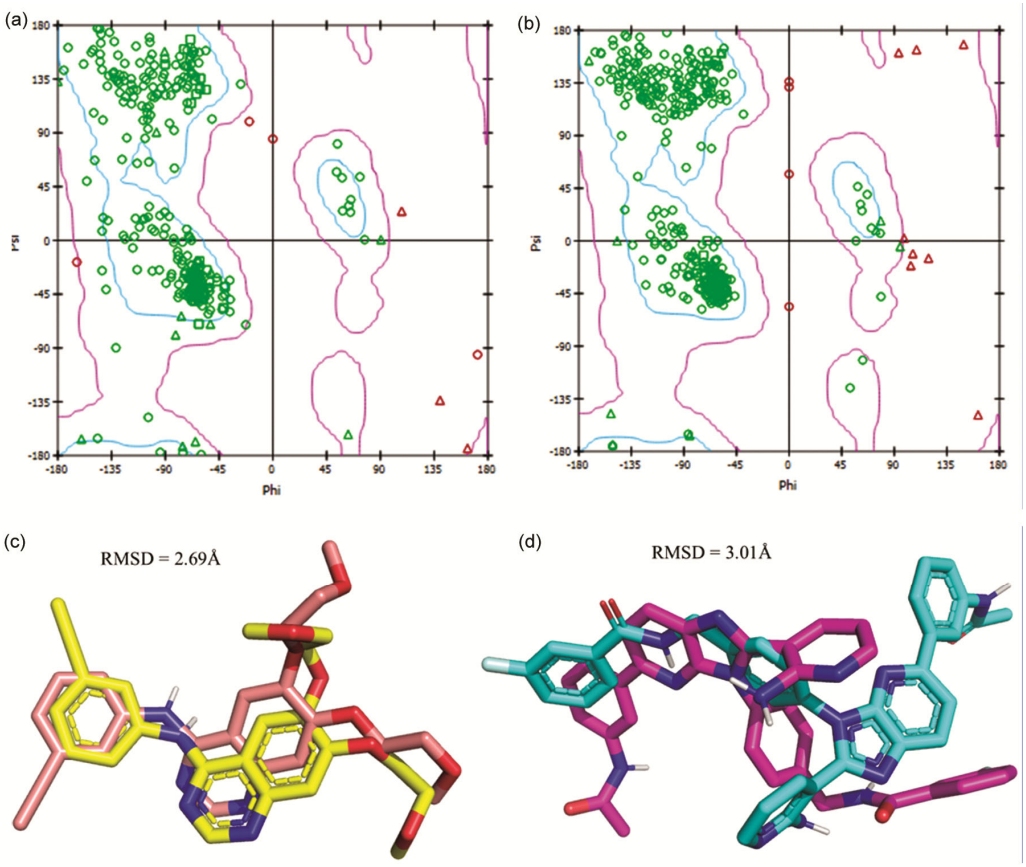

Fig. 1 — Ramachandran plot of (a) 1M17; (b) 4EJN; RMSD of redock co-crystal ligand of protein (c) EGRF; and (d) AKT1

Table 1 — Grid parameters & dimension, and binding site amino acids of protein EGFR and AKT1

Protein	Grid Dimension	Active site amino acids
EGFR (1M17)	center_x = 23.270785 center_y = -0.452346 center_z = 56.127430 size = 80 num_modes = 10 energy_range = 4	LEU 694, ALA 719, LEU 764, THR 766, GLN 767, LEU 768, MET 769, PRO 770, PHE 771, GLY 772, LEU 820, THR 830, ASP 831.
AKT1 (4EJN)	center_x = 32.804381 center_y = 46.493672 center_z = 18.870677 size = 80 num_modes = 10 energy_range = 4	ASN 53, ASN 54, GLN 59, LEU 78, GLN 79, TRP 80, ILE 84, MET 147, LYS 163, LEU 210, THR 211, ARG 222, VAL 270, VAL 271, TYR 272, ARG 273, ASP 274, ILE 290, ASP 292, TYR 326.

mode of binding of small molecules to their protein targets[28]. The acquired data was examined using BIOVIA Discovery Studio 2021. Discovery Studio facilitates the visualization of protein and ligand interactions in both 2D and 3D forms[28]. Surface style of the best docked poses was visualized in PyMOL v3.1.

We redocked the co-crystal ligand to the active site and compared the results with the original co-crystal ligand to obtain an accurate docking result (Fig. 1c & d). The root mean square deviation (RMSD) was calculated by PyMOL v3.1. The RMSD value was found to be less than 3.0Å, which suggests the validity of docking results[29].

Molecular dynamics (MD) simulations

1M17-quercetin-3,7-diglucoside complex showed significant binding energy and affinity. Therefore, we consider this complex for MD simulation. The structural stability of 1M17quercetin-3,7-diglucoside complexes was assessed by conducting 100 ns molecular dynamics

simulations using Desmond v2023-1 (Schrödinger, LLC, New York, NY). Systems were modeled with the OPLS_2005 force field and solvated in an orthorhombic TIP3P water box. The system was neutralized with 0.15 M NaCl. Energy minimization and equilibration steps were followed by NPT ensemble production runs. Analyses, including RMSD, root mean square fluctuation (RMSF), radius of gyration, principal component analysis (PCA), and H-bond fluctuations, were conducted using Simulation Interaction Diagram and Maestro v2023-1[30].

Binding free energy calculation

MM/GBSA is a computational method used to estimate the binding free energy between a protein and a ligand based on molecular dynamics simulation data. MM/GBSA combines molecular mechanics energies (MM), solvation effects using the generalized born (GB) model, and solvent-accessible surface area (SA) calculations. The MM/GBSA binding free energies were computed using the Prime MM/GBSA module in Maestro v2023-1 (Schrödinger, LLC). Frames from the last 20 ns of MD trajectories were extracted and evaluated using the VSGB 2.0 solvation model[31,32].

$$\Delta G(\text{bind}) = \Delta G(solv) + \Delta E(MM) + \Delta G(SA) \dots (A2)$$

where:

- Δ*G*solv is the difference in GBSA solvation energy of the EGFR-Quercetin-3,7-diglucoside complex and the sum of the solvation energies for unliganded EGFR and Quercetin-3,7-diglucoside.
- Δ*E*MM is a difference in the minimized energies between EGFR-Quercetin-3,7-diglucoside complex and the sum of the energies of the unliganded EGFR and Quercetin-3,7-diglucoside complex.
- Δ*G*SA is the difference in surface area energies of the complex and the sum of the surface area energies for the unliganded EGFR and Quercetin-3,7-diglucoside complex equation A2.

DFT analysis

Incorporating Koopmans' theorem and Parr's concept of chemical reactivity, the molecular descriptors of quercetin-3,7-diglucoside were obtained from DFT calculations. According to Koopmans' theorem, the ionization potential (IP) and electron affinity (EA) can be approximated by the negative values of the HOMO and LUMO energies, respectively[33]. DFT calculations were carried out using Gaussian 09 software with the B3LYP functional and 6-31G (d,p) basis set. The highest occupied molecular orbital- lowest unoccupied molecular orbital (HOMO-LUMO) energy levels, molecular electrostatic potential (MEP) maps, and chemical descriptors were calculated to evaluate electronic behavior and reactivity of top-ranked phytochemicals[34].

***In vitro* validation of anti-mitotic activity**

The anti-mitotic activity of *Hibiscus rosa-sinensis* extract was assessed using the Allium cepa root tip assay. Healthy onion bulbs were first surface-sterilized and allowed to sprout roots in distilled water under dark conditions for 48 h (Suppl. Fig. 1S). Once roots reached 1–2 cm, they were exposed to various concentrations of the plant extract (25, 50, 100, 200, and 400 µg/mL) for 24 h, while control bulbs remained in distilled water. Post-treatment, root tips were excised and fixed in a 3:1 solution of ethanol and glacial acetic acid for 24 h. The fixed roots were then hydrolyzed in 1N HCl at 60°C for 5 min to soften the tissue and subsequently stained with aceto-orcein to visualize chromosomal structures. The stained tips were compressed on microscope slides and examined at 100X magnification. At least 500 cells per slide were evaluated to assess the mitotic index (% of dividing cells). The observed decrease in mitotic index and increase in chromosomal anomalies provided strong evidence for the extract's anti-mitotic potential[35]. This method was selected because of the similarity between the onion root cells and human somatic cells. The following two equations A3 and A4,were used for calculation[36].

$$\%\ Inhibition = \frac{\text{Control}-\text{Treated}}{Control} x\ 100\% \dots (A3)$$

$$Mitotic\ index\ (MI) = \frac{\text{P+M+A+T}}{Total\ number\ of\ cells} x\ 100 \dots (A4)$$

P, M, A, and T are prophase, metaphase, anaphase, and telophase, respectively.

Statistical analysis

All experiments were conducted in triplicate (n = 3), and data was presented using mean ± SD. Graphs and statistical analysis were performed in Excel and Office 2016. To establish comparative validity, *In silico* and *in vitro* assays employed appropriate controls.

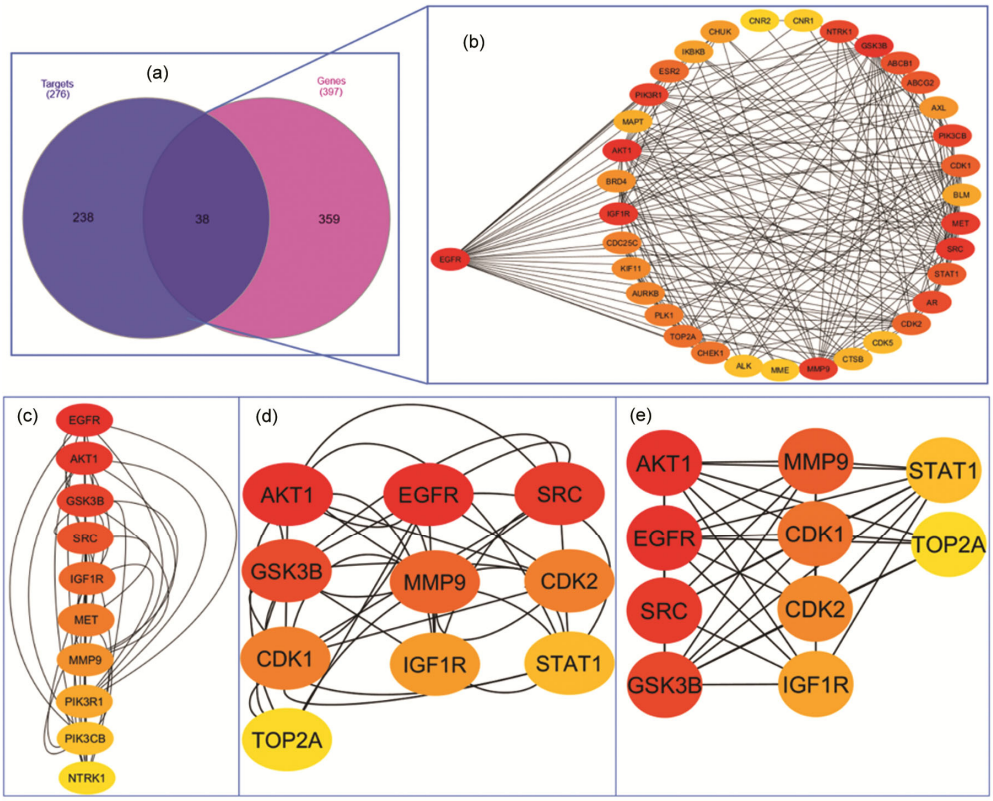

Fig. 2 — A common gene (a) Vann diagram; (b) PPI; top ten shortlists based on common genes using (c) MCC; (d) degree; and (e) closeness

Results

Extraction and phytochemical screening

The ethanolic extract yield of Hibiscus flower was 2.12% per 100 g of Hibiscus powder. The extract contained tannins, flavonoids, terpenoids, alkaloids, glycosides, carbohydrates, coumarins, quinones, and saponins.

Network pharmacology analysis

Hibiscus rosa-sinensis and mitosis-related genes suggested compound-associated targets for network pharmacology. Thus, 276 phytoconstituent targets and 397 mitosis-associated genes were identified. The Venn diagram (Fig. 2a) showed 38 genes intersecting, demonstrating molecular linkages between plant bioactive compounds and mitotic regulation.

The STRING database was used to generate a protein-protein interaction (PPI) network for these 38 overlapping genes, which appeared in Cytoscape. The network (Fig. 2b) included 37 nodes and 213 edges, compared to 98 expected by chance, suggesting significant integration. The network's average node degree was 11.5 and its local clustering coefficient was 0.668, indicating tight clusters. With a PPI enrichment p-value of < 1.0e-16, observed interactions were significant and not random.

To identify key targets, Maximal Clique Centrality (MCC) examined the top 36 genes. Top 10 hub genes (Fig. 2c) include EGFR, AKT1, GSK3B, SRC, IGF1R, MET, MMP9, PIK3R1, PIK3CB, and NTRK1, demonstrating their importance in the extract's biological activity. AKT1, EGFR, and SRC were significantly connected nodes in degree centrality analysis (Fig. 2d), whereas closeness centrality analysis (Fig. 2e) indicated them as critical regulators due to their proximity to other network nodes. These data support *Hibiscus rosa-sinensis* extract targeting essential mitotic signaling pathways by indicating a strong, non-random interaction network focusing on mitotic inhibition.

Functional enrichment analysis

Gene Ontology (GO) and Kyoto Encyclopedia of Genes and Genomes (KEGG) enrichment studies were undertaken to understand the biological relevance of the 38 frequent genes found by network pharmacology analysis. Enrichment analysis was also performed to further understand these targets'

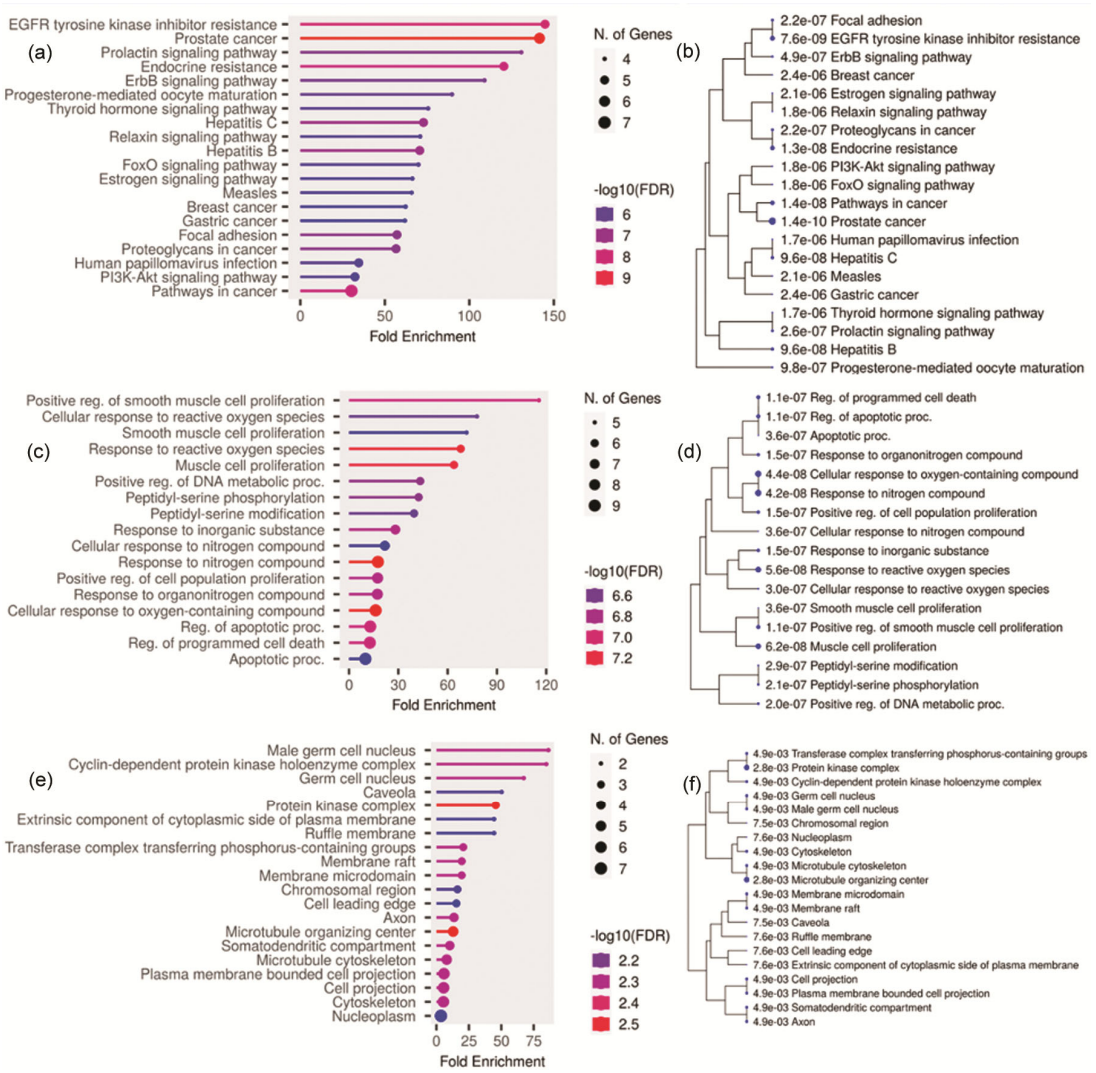

Fig. 3 — Fold enrichment analysis. Bar and tree plot of (a & b) KEGG; (c & d) bar and tree plot for GO biological; and (e & f) bar and tree plot of CC

biological activities. KEGG pathway analysis revealed significant enrichment in several cancer-associated and mitotic pathways, including EGFR tyrosine kinase inhibitor resistance, prostate cancer, endocrine resistance, prolactin signaling, ErbB signaling, PI3K-Akt signaling, and estrogen signaling pathways (Fig. 3a & b). High fold enrichment values (up to 150) and statistical significance (-log10 (FDR) values ≥7) indicate similar targets in oncogenic and mitotic signaling cascades.

GO analysis revealed complementary functional insights. Biological process (BP) enrichment (Fig. 3c & d) showed that the targets positively regulated smooth muscle cell proliferation, reactive oxygen species response, apoptosis, cell population proliferation, and peptidyl-serine phosphorylation. These findings show that targets regulate cell division and death. CC enrichment (Fig. 3e & f) demonstrated that the targets were localized in mitosis-related compartments such as the cyclin-dependent protein kinase holoenzyme complex, nucleoplasm, protein kinase complex, membrane rafts, and microtubule cytoskeleton. Their geographic distribution supports their mitotic control activity.

GO analysis revealed complementary functional insights. Biological process (BP) enrichment (Fig. 4a & b) showed that the targets positively regulated smooth muscle cell proliferation, reactive oxygen species response, apoptosis, cell population proliferation, and peptidyl-serine phosphorylation. These findings show that targets regulate cell division and death. CC enrichment (Fig. 4c & d) demonstrated that the targets were localized

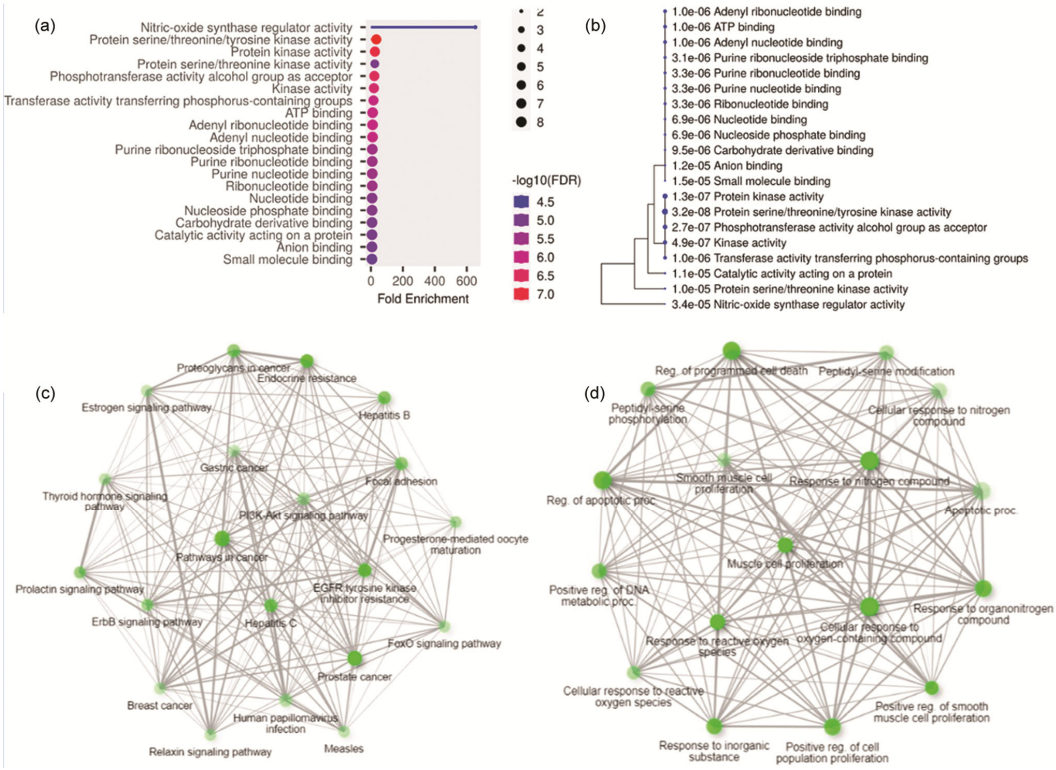

Fig. 4 — Fold enrichment analysis of (a & b) CF; network of (c) KEGG; and (d) GO biological

in mitosis-related compartments such as the cyclin-dependent protein kinase holoenzyme complex, nucleoplasm, protein kinase complex, membrane rafts, and microtubule cytoskeleton. Their geographic distribution supports their mitotic control activity.

Pathway analysis

The Figure 5 represents the KEGG pathway map for EGFR tyrosine kinase inhibitor (TKI) resistance. The red-highlighted boxes indicate genes or proteins that were identified as key targets in your study based on network pharmacology analysis.

EGFR tyrosine kinase inhibitor resistance

The EGFR tyrosine kinase inhibitor resistance pathway (KEGG hsa01521) outlines mechanisms by which cancer cells evade the effects of EGFR-targeted therapies such as gefitinib and erlotinib. In the pathway map, several critical genes are highlighted in red, including EGFR, ERBB2, ERBB3, IGF1R, PIK3R1, and GSK3B, all of which were identified as hub genes in the earlier PPI network analysis (Fig. 5).

Molecular docking

Molecular docking was performed on seven active constituents, the standard drug, and the co-crystal ligand against two protein targets EGFR protein (PDBIB:1M17) and the AKT1 protein (PDBID: 4EJN). The binding energies, interacting residues, and kinds of molecular interactions were examined to determine binding affinity and interaction patterns. The molecular docking method was validated using redocking with the co-crystallized ligands erlotinib (AQ4) and 0R4 attached to the EGFR and AKT1 proteins, respectively. Figure 6a & b are the presentation of 3D structure of the co-crystal ligand/reference drug erlotinib (AQ4) of 1M17 and 0R4 of 4EJN, respectively. Erlotinib itself is an EGFR inhibitor, therefore, we have used it as a reference drug for EGFR docking results analysis. Similarly, capivasertib is an AKT1 inhibitor used as a reference drug in our study.

Quercetin-3,7-diglucoside has shown a better binding affinity compared to the reference drug and co-crystal ligand for both proteins. For the EGFR target, all the compounds have shown good affinity except nicotinic acid when compared to the reference and co-crystal. Quercetin-3,7-diglucoside has the highest binding affinity with -9.6 Kcal/mol, whereas the reference drug and co-crystal ligand have binding

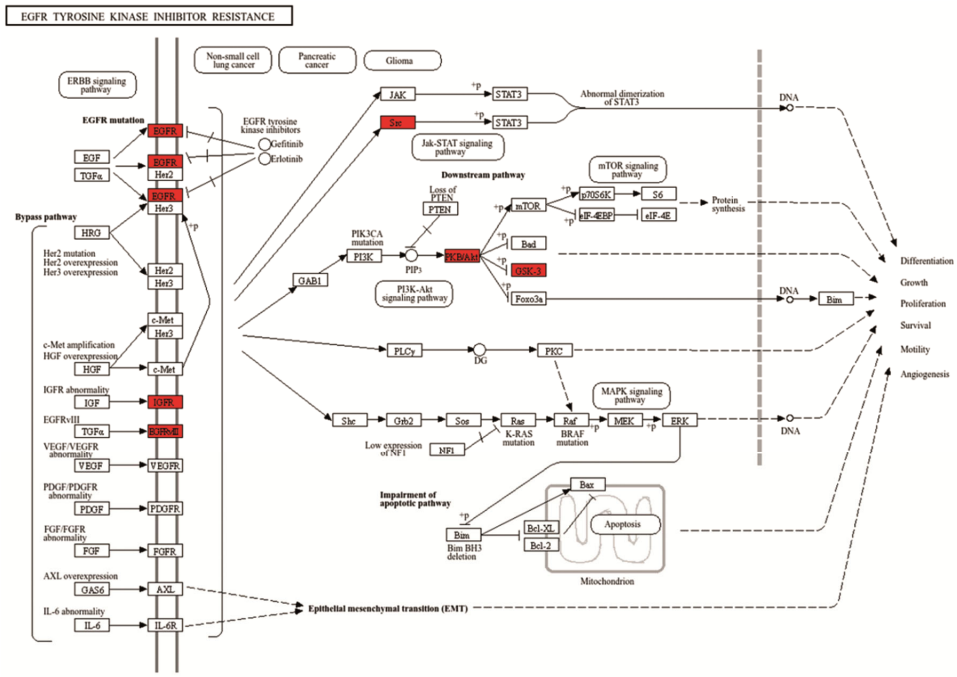

Fig. 5 — KEGG Pathway of EGFR tyrosine kinase inhibitor resistance (hsa01521). The pathway illustrates molecular mechanisms involved in resistance to EGFR-targeted therapies such as gefitinib and erlotinib. Red-highlighted nodes represent key target genes identified from network pharmacology and enrichment analyses. These targets are implicated in bypass signaling, downstream activation of the PI3K-Akt-mTOR and MAPK pathways, and impairment of apoptosis, all contributing to therapeutic resistance, cell survival, and tumor progression

energies of -7.4 Kcal/mol and -7.6 Kcal/mol, respectively (Table 2). Quercetin-3,7-diglucoside formed four hydrogen bonds with the amino acids MET 769, THR 766, LYS 721, and ASP 813 (Fig. 6c). The reference compound formed five hydrogen bonds with the amino acids TYR 803, ARG 807, SER 744, ARG 752, and GLN 677 (Table 2). Despite having fewer hydrogen bonds than the reference drugs, quercetin-3,7-diglucoside had the highest binding affinity, which might be attributed to the existence of pi-anion bonds. Even though the co-crystal ligand lacks a conventional hydrogen link, it has a higher binding energy than the reference, which might be attributed to the presence of Pi-Anion bonds.

On the target AKT1, quercetin-3,7-diglucoside has shown the best binding energy compared to the co-crystal ligand and reference drug capivasertib. Quercetin-3,7-diglucosideexhibited a binding energy of -11.0 Kcal/mol, whereas the co-crystal ligand showed a binding energy of -10.9 Kcal/mol and the reference drug capivasertib of -8.4 Kcal/mol. Quercetin-3,7-diglucosideshared the same pi-alkyl bonding with the reference drug on LEU 264 and Pi sigma bond with the co-crystal ligand on VAL 270 amino acid. Quercetin-3,7-diglucosidehas also formed 6 conventional hydrogen bonds with the protein (Fig. 6d). The presence of 6 conventional hydrogen bonds and pi-anion binding with amino acids made higher binding affinity. Whereas a co-crystal ligand with 3 conventional hydrogen bonds has shown good binding affinity that may be due to the presence of halogen bonding with amino acids. The 2D interaction of all the phytoconstituents against both the proteins is given in (Suppl. Fig. 2S to 16S).

MD simulation

Molecular docking results revealed that quercetin-3,7-diglucoside posed the highest binding affinity against AKT1 (4EJN). Therefore, we chose quercetin-3,7-diglucoside-AKT1 complex for MD simulation at a 100-ns timeframe.

RMSD and RMSF plot

The molecular dynamics simulation results revealed that the AKT1-Quercetin-3,7-diglucoside complex maintained structural stability throughout the 100 ns trajectory, as shown by the backbone RMSD, which plateaued around 2.4 Å after initial fluctuations (Fig. 7a). The ligand exhibited moderate flexibility, with RMSD values remaining below 2.8 Å, indicating stable

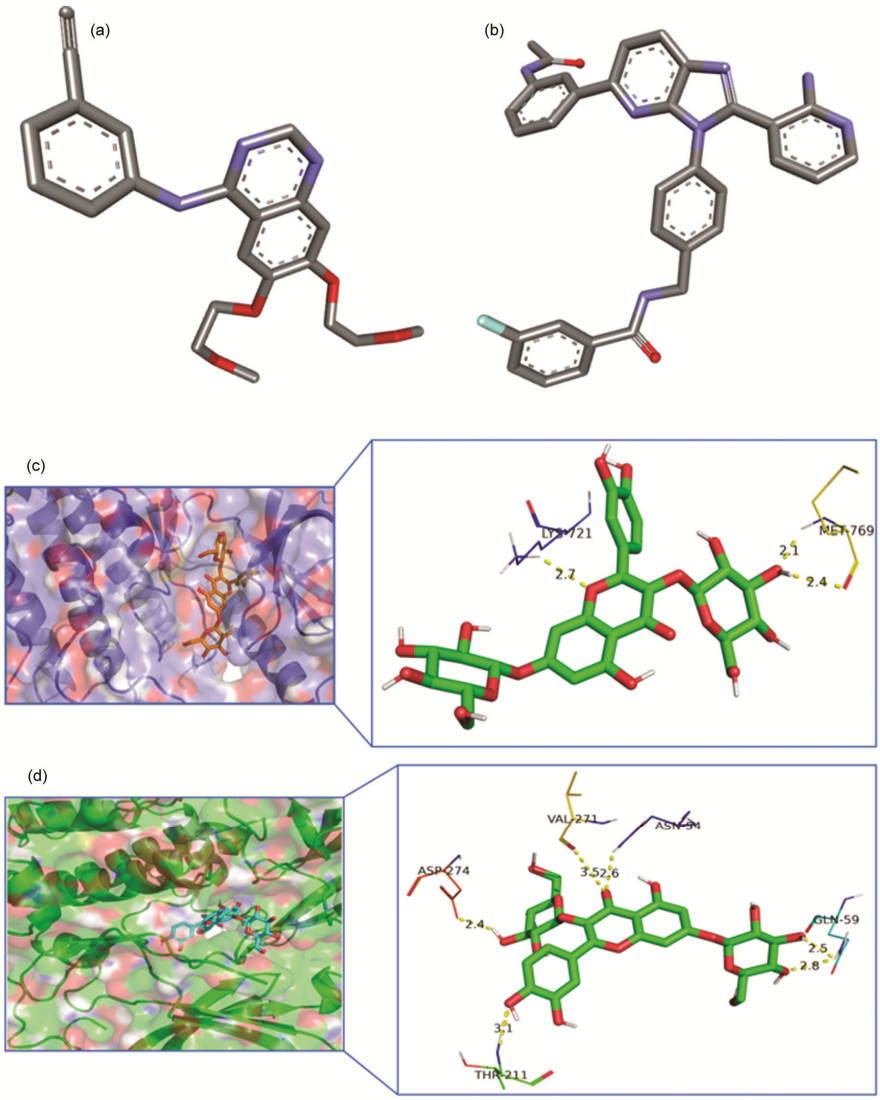

Fig. 6 — 3D structure of co-crystal ligand/reference drug erlotinib (AQ4) of (a) 1M17; (b) 0R4 of 4EJN; (c) Molecular docking interaction of quercetin-3,7-diglucoside against EGFR (1M17); and (d) AKT1 (4EJN)

binding within the active site. The Quercetin-3,7-diglucoside Root mean square fluctuation (RMSF) (Fig. 7b) showed relatively higher atomic fluctuations at the terminal atoms, suggesting local flexibility, whereas the protein RMSF (Fig. 7c) indicated that most residues remained stable with RMSF values under 2.0 Å, except for loop regions and terminal residues, which displayed peaks above 5.0 Å, reflecting expected flexibility in these dynamic regions.

Structural compactness and stability of complex

AKT1-Quercetin-3,7-diglucoside complex structure was consistent in molecular dynamics modeling. Protein structure remained compact throughout 100 ns, with a radius of gyration (Rg) range of 5.2 Å to 5.8 Å. A stable molecular surface area (MolSA) of around 490 Å² indicates little structural deformation. The solvent-accessible surface area (SASA) fell from ~170 Å² to ~150 Å² in the first 60 ns, but steadily increased to ~200 Å² by the conclusion of the simulation, suggesting considerable solvent exposure (Fig. 8a). Polar surface area (PSA) remained stable at 460-500 Å². Secondary structure elements (SSE) analysis confirmed the stability of α-helices and β-sheets in the protein, with a 42% percentage of secondary structure content throughout the simulation period (Fig. 8b).

Protein-ligand contact

AKT1-quercetin-3,7-diglucoside contact study showed persistent contacts over 100 ns. The

Table 2 — Binding energy, interacting amino acids, and number of hydrogen bonds.

S. No	Phytoconstituents	Binding Energy (kcal/mol)	Interacting Amino Acids	Number of H-bonds
		EGFR (PDBID: 1M17)		
1	Nicotinic acid	-5.3	ASP 831, MET 742, ALA 719, LYS 721	1
2	Quercetin-3,7-diglucoside	-9.6	MET 769, THR 766, LYS 721, ASP 813, ASP 831, PHE 699, VAL 702, ALA 719	3
3	Kaempferol-3-xylosylglucoside	-9.5	ARG 817, GLU 738, LEU 820, LYS 721, THR 766, ALA 719, GLY 772, LEU 694, VAL 702	5
4	Quercetin-3-sophorotrioside	-8.7	LYS 721, MET 769, CYS 773, PRO 770, GLY 772, ARG 817	7
5	Quercetin	-8.9	MET 769, GLN 767, ASP 831, THR 830, MET 742, VAL 702, LEU 820, LEU 694, ALA 719, LYS 721	5
6	Cyanine	-9.4	ARG 817, ASP 813, ASP 831, ALA 719, MET 769, THR 766, LEU 694, LEU 820, VAL 702	5
7	β-Sitosterol	-8.7	LYS 721, VAL 702, LEU 694	-
8	Erlotinib (reference drug/co-crystal ligand)	-7.6	LEU 820, GLU 738, VAL 702, ASP 831, PHE 699	-
		AKT1 (PDBID: 4EJN)		
1	Nicotinic acid	-5.4	THR 211, SER 205, ASO 292, TRP 80	3
2	Quercetin-3,7-diglucoside	-11.0	GLN 79, ASN 54, TYR 272, ASP 274, THR, 211, GLN 59, ASP 292, VAL 270, TRP 80, LEU 210, LEU 264	6
3	Kaempferol-3-xylosylglucoside	-10.5	ALA 58, LEU 78, GLN 203, GLU 267, GLN 59, ASN 53, VAL 270, GLN 79, TRP 80	6
4	Quercetin-3-sophorotrioside	-8.0	GLN 59, ASN 53, GLU 267, ALA 58, LEU 78, GLN 203, VAL 270, GLN 79, TRP 80	6
5	Quercetin	-9.4	SER 205, VAL 271, GLN 79, ASP 292, TRP 80, LEU 210	3
6	Cyanine	-9.6	GLN 203, LYS 268, THR 82, GLN 79, THR 291, THR 211, ASP 292, TYR 272, LEU 264, TRP 80, VAL 270, LEU 210	6
7	β-Sitosterol	-9.2	THR 291, THR 211, LEU 202, TRP 80, LEU 210, LEU 264	2
8	Capivasertib (Reference drug)	-8.4	ASN 53, LYS 60, 77, ALA 58, TRP 80, LEU 264, VAL270	-
9	Co-crystal (0R4)	-10.9	ASP 292, ASN 53, ASP 32, TRP 90, VAL 270, LYS 268, GLN 59, ALA 58	3

histogram (Fig. 9a) demonstrated that THR80, GLU104, GLU117, and ASP293 often contacted the ligand. THR80 had the highest cumulative contact count, reaching 2.0, followed by GLU104 and ASP293. The contact history (Fig. 9b) demonstrated continued interaction with 10–20 contacts. The heatmap showed that residues such as THR80, GLU104, and ASP293 exhibited several and sustained interactions (≥3 contacts) across frames, confirming their role in ligand stabilization. At the active site, ligand binding is stable and persistent.

Post-simulation analysis

PCA and FEL mapping examined MD simulated conformational dynamics. The 2D FEL plot (Fig. 10) showed multiple well-defined low-energy basins with free energy minima of roughly 3.5 kcal/mol, predominantly along PC1 and PC2 axes, indicating at least three dominant stable states. The 3D FEL (Fig. 10) reveals energy minima at 16 kcal/mol and maxima at 26 kcal/mol, indicating significant energetic barriers (~10 kcal/mol) between structural components. The 3D PCA projection (bottom left) showed the temporal development of the system over PC1, PC2, and PC3, with a color gradient indicating simulation time (0 to ~80,000 ps). It also indicated conformational transitions between clustered states. PC1 had multimodal peaks at -50, 0, and 75, while PC2 had a dominant peak near 0, indicating that PC1 caught the significant conformational variability and transitions (Fig. 10).

MM/GBSA energy calculation

The MM/GBSA study showed a steady ligand-protein binding affinity during the 100 ns simulation.

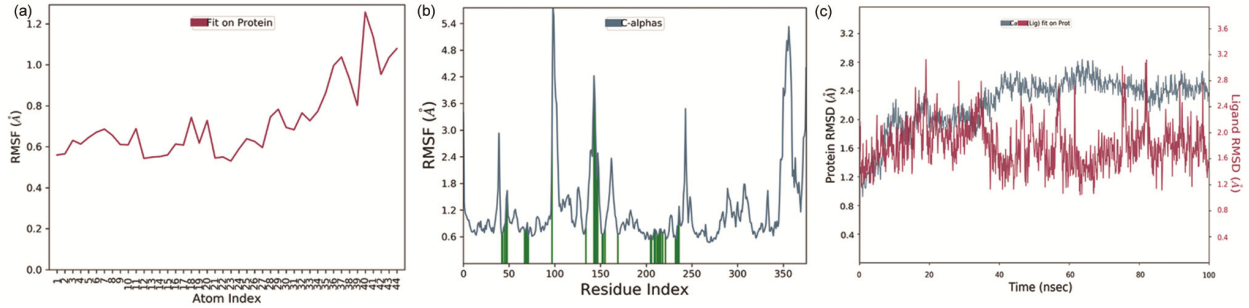

Fig. 7 — (a) RMSD plot of AKT1 (blue) and ligand (red) stability throughout 100 ns of simulation; (b) Ligand atom RMSF plot showing local flexibility; and (c) Protein residue RMSF plot showing dynamic flexibility of terminal and loop regions with higher fluctuations

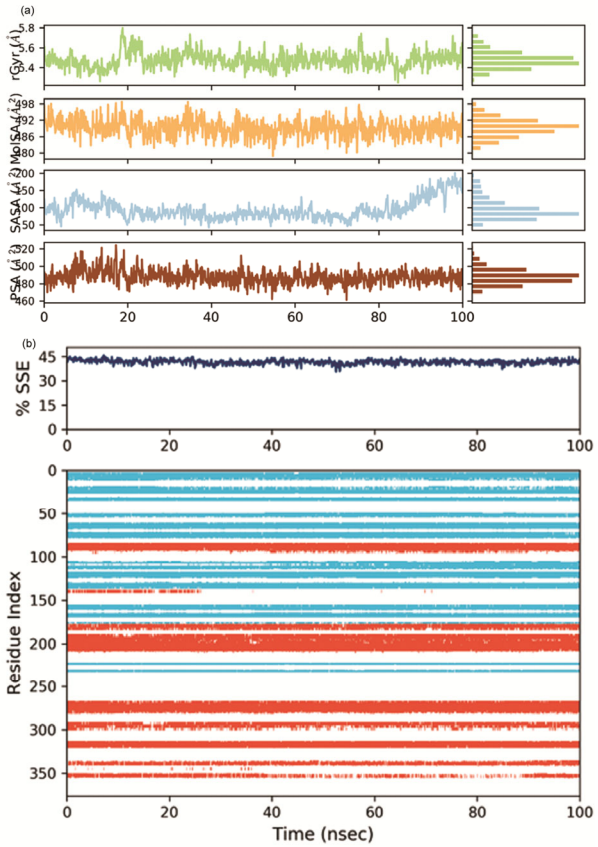

Fig. 8 — (a) AKT1–Quercetin-3,7-diglucoside complex Rg, MolSA, SASA, and PSA time evolution during the 100 ns MD simulation. Histograms on the right show simulated parameter distributions. The SSE timeline; and (b) displays the distribution of α-helices (red) and β-sheets (blue) across residue indices across time, with the proportion of SSE suggesting constant structural integrity

Figure 11a shows a constant ΔG_bind trajectory oscillating at -73.14 kcal/mol, indicating a stable interaction. The box plot (Fig. 11b) demonstrated that van der Waals and Coulomb forces increased binding energy, whereas lipophilic, hydrogen bonding, and covalent interactions supported it. Histogram graphs (Fig. 11c) confirmed the typical energy distribution,

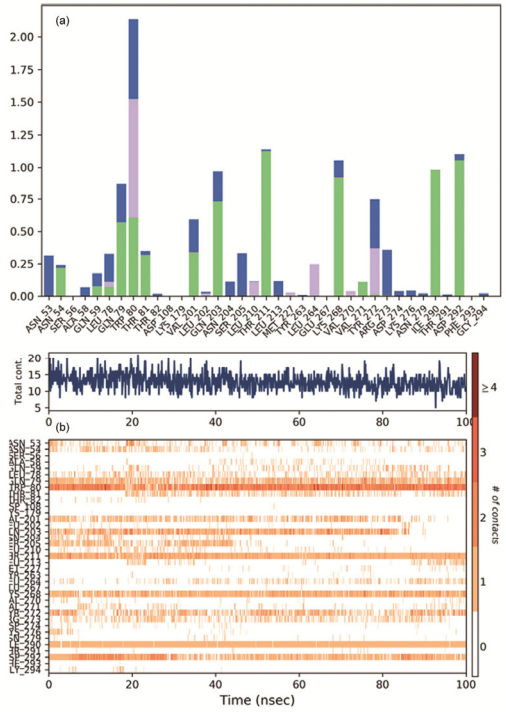

Fig. 9 — AKT1-quercetin-3,7-diglucoside contact (a) histogram; and (b) timeline

with ΔG_bind peaking at -73 to -75 kcal/mol. These findings suggest a strong and energy-efficient AKT1-quercetin-3,7-diglucoside interaction.

DFT analysis

DFT calculations of quercetin-3,7-diglucoside indicate its molecular properties in (Table 3). There was a 3.648 eV energy difference between HOMO and LUMO energy levels of -0.07662 a.u. (2.086 eV) and -0.21057 (5.734 eV), suggesting moderate chemical reactivity and kinetic stability. Both ionization potential and electron affinity were 2.086 and 5.734 eV. The molecule possesses 3.910 electronegativity and -3.910 eV chemical potential. Negative chemical hardness (-1.824 eV) and

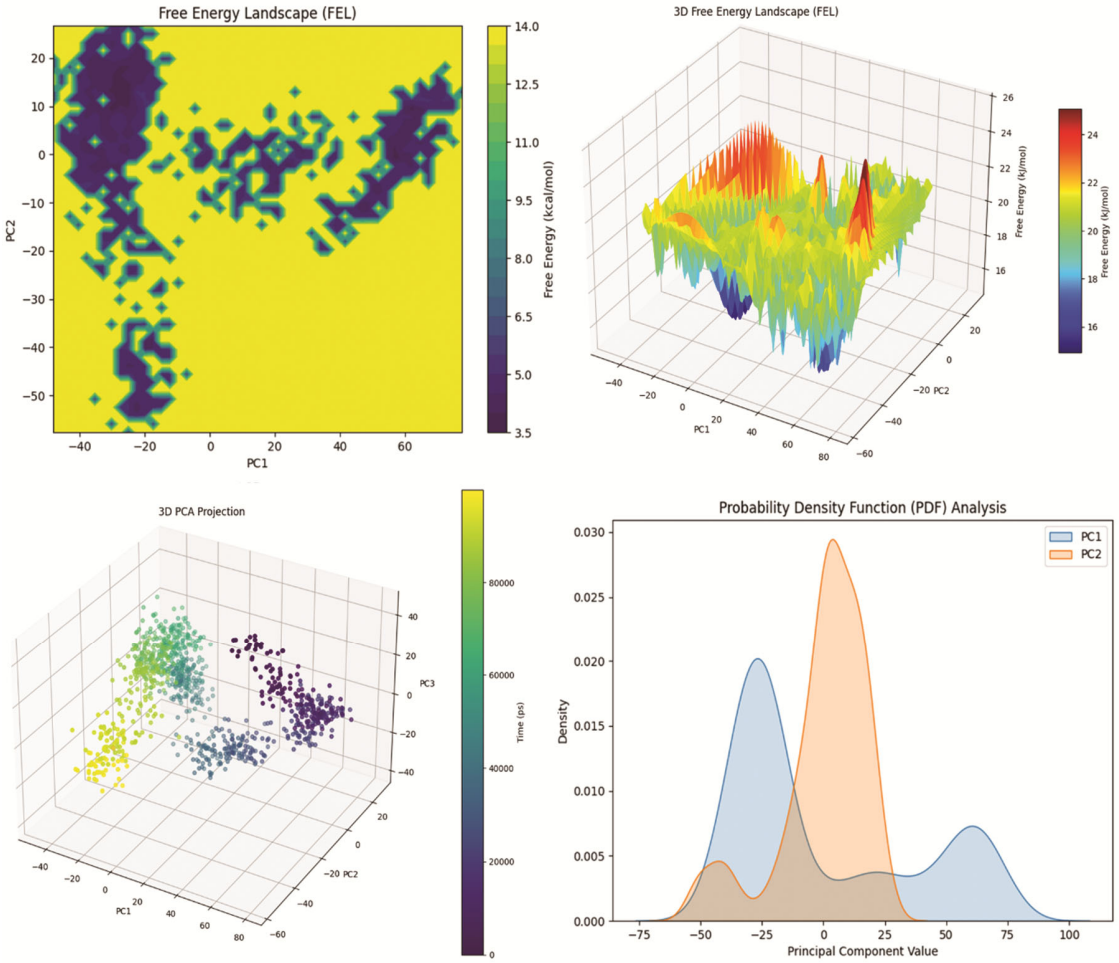

Fig. 10 — Post-MD simulation conformational analysis using PCA and FEL methods

electrophilicity (-4.189) suggested an unusual electronic configuration or calculation aberration. Additionally, the compound's -0.548 eV^{-1} chemical softness implies potential reactivity. These descriptions showed the compound's electrical and reactivity.

Figure 12 illustrates the electrostatic potential (ESP) surface, highest occupied molecular orbital (HOMO), and lowest unoccupied molecular orbital (LUMO) of quercetin-3,7-diglucoside as derived from density functional theory (DFT) calculations. The ESP map (Fig. 12a) displayed a heterogeneous charge distribution across the molecule, with red regions signifying elevated electron density around the hydroxyl and carbonyl oxygen atoms, indicating potential locations for electrophilic assault. Blue regions exhibited electron deficiency, promoting nucleophilic interactions. The HOMO distribution (Fig. 12b) mostly concentrated on the flavonoid core, particularly surrounding aromatic rings and hydroxyl groups, signifying increased electron donation. The LUMO distribution (Fig. 12c) concentrated around aromatic rings and extended towards glycosidic moieties, indicating their potential to accept electrons during interactions. The spatial overlap between the HOMO and LUMO regions indicates π-π* transitions and intramolecular charge transfer. These visualizations corroborated DFT-derived chemical descriptors and demonstrated the molecule's redox and hydrogen bonding capabilities.

***In vitro* validation of anti-mitotic activity**

Anti-mitotic activity of *Hibiscus rosa-sinensis* extract was investigated using the Allium cepa root meristem model. Growth suppression was dose-dependent, with mean root length decreasing by 76.3% from 3.21 ± 0.15 cm in control to 0.76 ± 0.06 cm at 400 µg/mL (Table 4). Microscopic analysis of dyed root tips revealed a substantial drop in mitotic

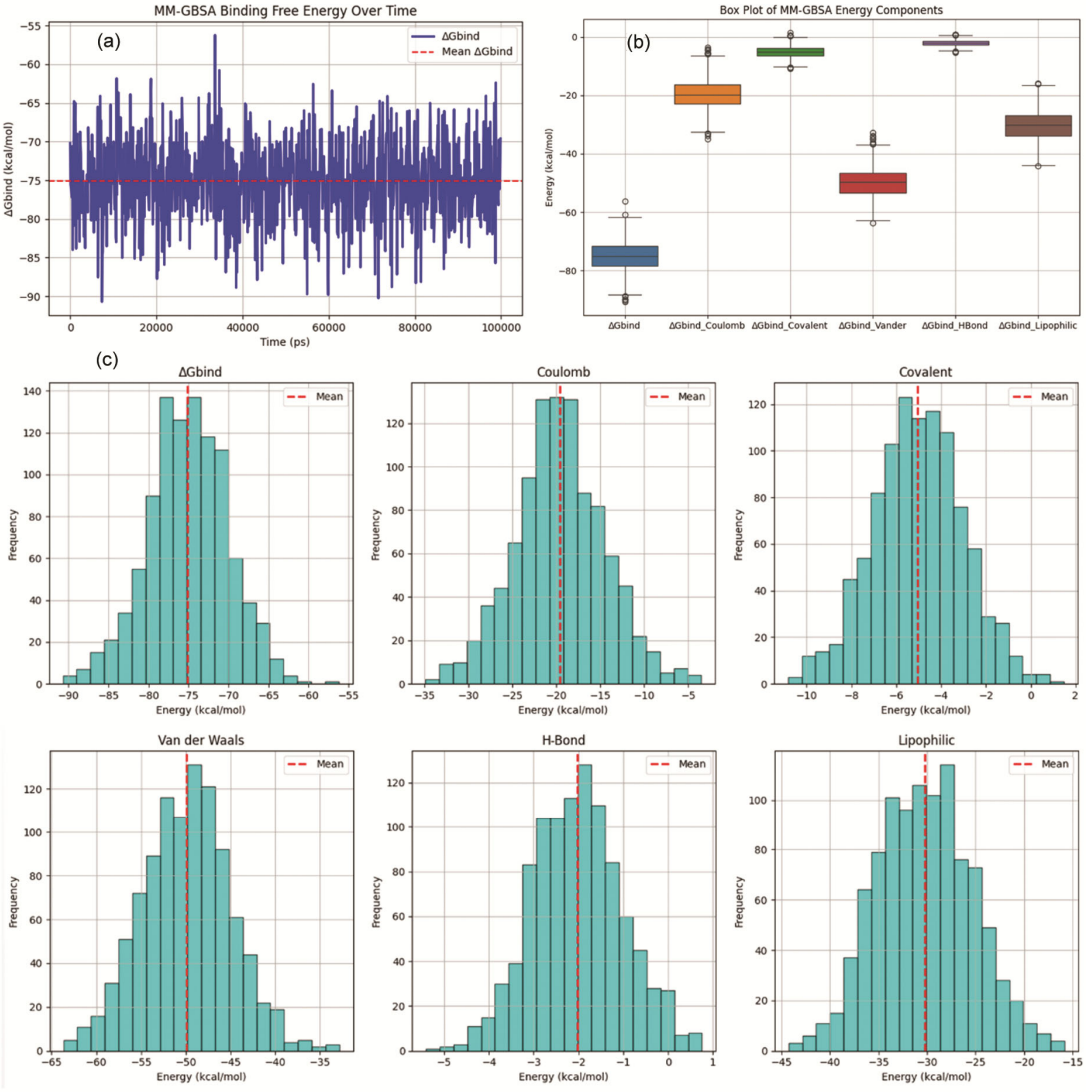

Fig. 11 — (a) MM/GBSA binding free energy over time; (b) box plot of MM/GBSA energy component; and (c) MM/GBSA energy histogram

Table 3 — Molecular descriptors of quercetin-3,7-diglucoside from DFT calculation.

S. No	Property	Value (eV)
1	HOMO	–0.07662 a.u. = 2.086
2	LUMO	–0.21057 a.u. = 5.734
3	Ionisation Potential	2.086
4	Electron Affinity	5.734
5	Electronegativity	3.910
6	Chemical Hardness	–1.824
7	Chemical Potential	–3.910
8	Chemical Softness	–0.548 eV^{-1}
9	Electrophilicity	–4.189
10	Energy Gap	3.648

Table 4 — Percentage inhibition of *Hibiscus rosa-sinensis* flower extract at different concentrations.

Concentration (µg/mL)	Mean Root Length (cm) ± SD	% Inhibition
Control	3.21 ± 0.15	0
50	2.68 ± 0.12	16.5
100	1.91 ± 0.09	40.5
200	1.23 ± 0.07	61.7
400	0.76 ± 0.06	76.3

index (MI) from 16.2% in control to 2.6% at 400 µg/mL extract concentration (Table 5). C-mitosis, chromosomal bridges, stickiness, and laggards increased throughout time. Mitosis abnormalities

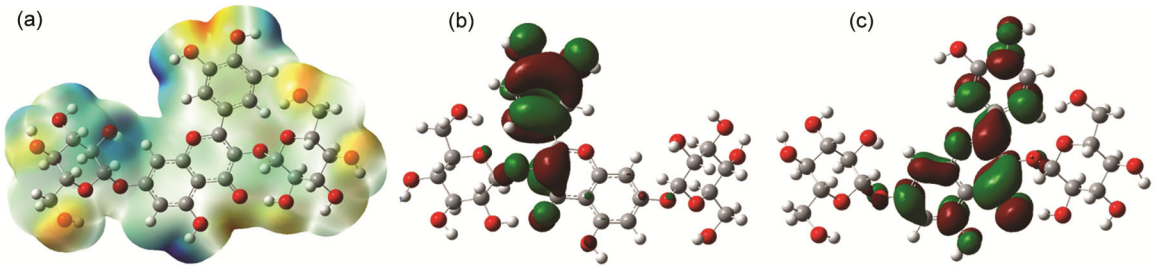

Fig. 12 — (a) ESP; (b) HOMO, and (c) LUMO of quercetin-3,7-diglucoside

Table 5 — Mitotic index and mitotic inhibition of extract by onion root method

Concentration (µg/mL)	Total Cells Counted	Dividing Cells	Mitotic Index (%)	Abnormal Mitoses (%)
Control	500	81	16.2	1.2
50	500	62	12.4	5.3
100	500	41	8.2	9.5
200	500	25	5	13.8
400	500	13	2.6	18.7

elevated from 1.2% in controls to 18.7% in the 400 µg/mL group. The extract inhibited spindle formation and chromosomal segregation during cell division, proving its powerful anti-mitotic actions.

Discussion

This study highlights the therapeutic promise of *Hibiscus rosa-sinensis* through an integrative *in vitro* and *in silico* molecular docking and network pharmacology approach. Cancer is defined by aberrant cell proliferation that has a tendency to multiply unchecked, advancing from a precancerous lesion to a malignant condition. It is one of the leading causes of death globally. Reports have shown that by 2030, there will likely be 1.7 million annual cancer deaths and nearly 2.6 million new cases[37]. Treatment options for cancer exist. Surgery and chemotherapy can cause significant adverse effects and medication resistance, decreasing their efficacy. This has increased the quest for safer, more effective alternatives. Natural goods, especially ethnomedical plants, may help design biocompatible, less harmful cancer treatments[38]. *Hibiscus rosa-sinensis* active chemicals alter cancer progression regulators such kinases and growth factor receptors, suggesting multi-targeted mitotic and survival signaling interference. The convergence of enriched pathways and tightly coupled protein interactions may disrupt resistance mechanisms, including EGFR inhibitor escape. The targets range from upstream receptors to downstream effectors, suggesting broad-spectrum modulation rather than single-node suppression. These findings encourage rationally exploring *Hibiscus rosa-sinensis* as an anticancer candidate to overcome treatment resistance and regulate unrestrained growth.

Mechanism of action

Upstream activation and bypass mechanisms

EGFR and its family members (ERBB2 and ERBB3) are receptor tyrosine kinases that start downstream signaling upon ligand activation. These receptors' overexpression or mutation activates proliferative and survival pathways. Cancer cells can also overcome EGFR suppression by activating parallel pathways including the PI3K-Akt axis via IGF1R[39–41].

Downstream signaling: PI3K-Akt-mTOR and MAPK pathways

The red PIK3R1, a regulatory subunit of PI3K, stimulates downstream kinases including Akt, phosphorylating and inactivating GSK3B. This increases tumor cell survival and decreases apoptosis. In EGFR-mutated tumors, the PI3K-Akt-mTOR cascade is a well-known survival pathway and a frequent resistance mediator.

Functional implications

Activating these pathways phosphorylates transcription factors and apoptotic inhibitors, causing uncontrolled cell proliferation, survival, and therapeutic resistance. Genes like GSK3B regulate cellular metabolism and death, whereas PIK3R1 links membrane receptor function to intracellular signaling. JAK-STAT, MAPK, and mTOR pathways activate together, promoting tumor development, metastasis, and resistance. The phytochemical-target network hub targets EGFR, ERBB2, ERBB3, IGF1R, PIK3R1, and

GSK3B regulate the EGFR-TKI resistance pathway, according to the KEGG map. *Hibiscus rosa-sinensis* phytocompounds may target bypass signaling, anti-apoptotic survival pathways, and treatment resistance to change crucial resistance nodes and restore EGFR inhibitor sensitivity.

Docking and *in vitro* anti-mitotic activity

The docking results indicated significant interactions between Select *Hibiscus rosa-sinensis* phytochemicals and two key mitotic regulators, EGFR (1M17) and AKT1 (4EJN). Quercetin-3,7-diglucoside had the highest binding affinity for EGFR (-9.6 kcal/mol) and AKT1 (-11.0 kcal/mol), forming many hydrogen bonds with critical amino acid residues, indicating potential inhibition of both targets. The quercetin-3,7-diglucoside molecule exhibited stability, with an average hydrogen bond distance of 2.4 Å (1M17) and 2.8 Å (4EJN). Kaempferol-3-xylosylglucoside and cyanine exhibited robust binding to both proteins, with docking scores ranging from -9.4 to -10.5 kcal/mol and forming up to six hydrogen bonds, signifying stable and specific interactions. Quercetin, a prominent flavonoid, exhibited moderate binding to both targets with favorable interaction patterns. Numerous molecules have greater binding energy than co-crystallized ligands, indicating potential for therapeutic applications. Multiple hydrogen bonds and contact with significant residues like LYS 721, ASP 831 (EGFR), and TRP 80, GLN 79, ASP 292 (AKT1) demonstrate the mechanistic importance of these phytochemicals in mitotic signaling.

The extract significantly inhibited root growth in *Allium cepa* in a dose-dependent manner, with 76.3% inhibition observed at 400 µg/mL. Correspondingly, the mitotic index decreased markedly from 16.2% in the control to 2.6% at the highest concentration, indicating effective suppression of cell division. *V. harini* used MTT (3- [4,5-dimethylthiazol-2-yl]-2,5 2,5-diphenyl tetrazolium bromide) assay to assess *Hibiscus rosa-sinensis* anticancer property, and the results indicated a concentration-dependent reduction in cell growth and proliferation. Promising anticancer potential was shown by the extract, which may help slow the spread of cancer[10]. Furthermore, the Ag nanoparticles by *Hibiscus rosa-sinensis* extract also showed significant dose dependent antiproliferative activity[42]. The activity toward the cancer cell is due to the presence of low molecular weight component in the extract[11].

The mitotic phases and chromosomal abnormalities in *Allium cepa* root tip cells stained to observe nuclear and chromosomal dynamics. The presence of several abnormal mitotic visual suggests interference in the normal cell division process. C-mitosis, characterized by scattered chromosomes without spindle organization, indicates disruption of spindle fiber formation, often associated with anti-mitotic agents[43]. Chromosome bridges result from improper chromatid separation, typically due to DNA damage or improper repair. Laggards refer to chromosomes that fail to migrate properly during anaphase, increasing the risk of aneuploidy[44]. The formation of micronuclei and sticky chromosomes, seen in the last panel, reflects genotoxic stress and chromosomal instability, which are hallmarks of anti-mitotic and cytotoxic activity.

The mitotic aberrations suggest that *Hibiscus rosa-sinensis* flower extract may influence spindle formation, chromosomal segregation, or kinetochore functionality. Disruptions validate the extract's cellular anti-mitotic and anti-proliferative properties, endorsing its further investigation as a potential cancer therapy option. Molecular docking revealed that quercetin-3,7-diglucoside and kaempferol-3-xylosylglucoside have significant binding affinity to the mitosis-related targets EGFR and AKT1. Numerous hydrogen bonds with essential residues maintained these connections, as demonstrated by MM/GBSA and dynamic simulations. MM/GBSA analysis indicated stable binding (ΔG_bind -74.06 kcal/mol), mostly attributable to van der Waals (-45.85) and lipophilic (-26.53) interactions. The combination of *in vitro*, *in silico*, and cytogenetic data substantiates the extract's promise as a natural anti-mitotic compound aimed at inhibiting cancer cell proliferation.

Limitation and future prospective

This study combines network pharmacology, molecular docking, MM/GBSA simulations, and DFT calculations to forecast the interaction of phytoconstituents from *Hibiscus rosa-sinensis* with essential mitosis-regulating proteins (EGFR and AKT1). Nevertheless, these outcomes are prognostic in nature and need functional validity. No *in vitro* or in-vivo research has substantiated the inhibition of the EGFR/AKT pathway. Current work is limited by this. The computational findings justify additional investigation and provide early insights that might help build tailored biological experiments. The extract includes numerous bioactive compounds, and their

individual contributions to the reported activity are unknown. The pharmacokinetic and toxicological properties of the lead compounds, crucial for medicinal development, were not examined.

Identifying the extract's key active ingredients should be followed by rigorous in-vivo evaluation to demonstrate its efficacy and safety. Pharmacological methods through gene and protein expression analysis will elucidate their anti-mitotic functions. Structure-activity relationship (SAR) investigations and formulation development may help optimize these compounds for cancer therapy.

Conclusion

In vitro and *in silico* investigations show that *Hibiscus rosa-sinensis* extract has promising anti-mitotic effects. Network pharmacology, molecular docking, MM/GBSA simulations, and DFT computations revealed bioactive compound-mitotic target interactions. Quercetin-3,7-diglucoside's stability and binding characteristics make it a promising cancer cell proliferation treatment. *In vivo* confirmation is needed, however *Hibiscus rosa-sinensis* may be useful for developing plant-based anti-cancer therapies.

Acknowledgement

We thank Nargund College of Pharmacy and Honeychem Pharma Research Ltd. in Bangalore, India, for providing spectral analysis.

Conflict of interest

All authors declare no conflict of interest.

References

1 Morgan E, Arnold M, Gini A, Lorenzoni V, Cabasag CJ, Laversanne M & Soerjomataram I, Global burden of colorectal cancer in 2020 and 2040: incidence and mortality estimates from GLOBOCAN. *Gut*, 72 (2023) 338.

2 WHO, Global cancer burden growing, amidst mounting need for services. WHO, 45 (2024) 326.

3 Levine MS & Holland AJ, The impact of mitotic errors on cell proliferation and tumorigenesis. *Genes Dev*, 32 (2018) 620.

4 Otto T & Sicinski P, Cell cycle proteins as promising targets in cancer therapy. *Nat Rev Cancer*, 17 (2017) 93.

5 Ma C & Gurkan-Cavusoglu E, A comprehensive review of computational cell cycle models in guiding cancer treatment strategies. *npj Syst Biol Appl*, 10 (2024) 1.

6 Singh SS, Kumari M & Sharma M, A review on *Hibiscus rosa-sinensis*, extraction and its pharmacological activity. *Int J Res Anal Rev*, 11 (2024) 864.

7 Munir N, Khilji SA, Rasool S, Khalil A & Sajid ZA, Phytochemical analysis, antibacterial, and antitumor potential of *Hibiscus rosa-sinensis* Linn. *Scientifica (Cairo)*, 2025 (2025) 1.

8 Zulkurnain EI, Ramli S, Ali AA, James RJ, Kamarazaman IS & Halim H, The phytochemical and pharmacological effects of *Hibiscus rosa-sinensis*: a review. *Int J Pharm Investig*, 13 (2023) 422.

9 Mitra D, Saha M & Chatterjee S, A mini review on phytochemical and therapeutic potentiality of Hibiscus: an ornamental plant species. *J Med Plants Stud*, 12 (2024) 63.

10 Harini VS, Evaluation of the anticancer, antidiabetic, and *in vitro* wound healing properties of the aqueous and ethanolic extract of *Hibiscus rosa-sinensis* L. *J Pharm Bioallied Sci*, 16 (2024) S1217.

11 Goldberg KH, Yin AC, Mupparapu A, Retzbach EP, Goldberg GS & Yang CF, Components in aqueous *Hibiscus rosa-sinensis* flower extract inhibit *in vitro* melanoma cell growth. *J Tradit Complement Med*, 7 (2017) 45.

12 Vetrivel P, Murugesan R, Bhosale PB, Ha SE, Kim HH, Heo JD & Kim GS, A network pharmacological approach to reveal the pharmacological targets and its associated biological mechanisms of prunetin-5-o-glucoside against gastric cancer. *Cancers (Basel)*, 13 (2021) 1.

13 Quayum ST, Esha NJI, Siraji S, Abbad SSA, Alsunaidi ZHA, Almatarneh MH & Rahman M, Exploring the effectiveness of flavone derivatives for treating liver diseases: utilizing DFT, molecular docking, and molecular dynamics techniques. *MethodsX*, 12 (2024) 102537.

14 Agu PC, Afiukwa CA, Orji OU, Ezeh EM, Ofoke IH, Ogbu CO & Uche N, Molecular docking as a tool for the discovery of molecular targets of nutraceuticals in diseases management. *Sci Rep*, 13 (2023) 1.

15 Genheden S & Ryde U, The MM/PBSA and MM/GBSA methods to estimate ligand-binding affinities. *Expert Opin Drug Discov*, 10 (2015) 449.

16 Pandey B, Thapa S, Biradar MS, Singh B, Ghale JB, Kharel P & Ghimire L, LC-MS profiling and cytotoxic activity of Angiopterishelferiana against HepG2 cell line: molecular insight to investigate anticancer agent. *PLoS One*, 19 (2024) 1.

17 Pandey B, Thapa S, Kaundinnyayana A & Panta S, Hepatoprotective effects of Juglans regia on carbon tetrachloride-induced hepatotoxicity: *In silico*/*in vivo* approach. *Food Sci Nutr*, 12 (2024) 6482.

18 Heberle H, Meirelles VG, da Silva FR, Telles GP & Minghim R, InteractiVenn: a web-based tool for the analysis of sets through Venn diagrams. *BMC Bioinformatics*, 16 (2015) 1.

19 Lee K, Choi YJ, Lim HI, Cho KJ, Kang N & Ko SG, Network pharmacology study to explore the multiple molecular mechanism of SH003 in the treatment of non-small cell lung cancer. *BMC Complement Med Ther*, 24 (2024) 1.

20 Otasek D, Morris JH, Bouças J, Pico AR & Demchak B, Cytoscape Automation: empowering workflow-based network analysis. *Genome Biol*, 20 (2019) 1.

21 Ge SX, Jung D & Yao R, ShinyGO: a graphical gene-set enrichment tool for animals and plants. *Bioinformatics*, 36 (2020) 2628.

22 O'Boyle NM, Banck M, James CA, Morley C, Vandermeersch T & Hutchison GR, Open Babel: an open chemical toolbox. *J Cheminform*, 3 (2011) 1.

23 Baby K, Maity S, Mehta CH, Nayak UY, Shenoy GG, Pai KSR & Shukla R, Computational drug repurposing of

Akt-1 allosteric inhibitors for non-small cell lung cancer. *Sci Rep*, 13 (2023) 1.
24 Stamos J, Sliwkowski MX &Eigenbrot C, Structure of the epidermal growth factor receptor kinase domain alone and in complex with a 4-anilinoquinazoline inhibitor. *J Biol Chem*, 277 (2002) 46265.
25 Ashwell MA, Lapierre JM, Brassard C, Bresciano K, Bull C, Cornell-Kennon S & Keats JJ, ArQule Inc., 19 Presidential Way, Woburn, Massachusetts 01801, United States. *J Med Chem*, 55 (2012) 5291.
26 Prasad S, Kurmi C, Thapa S & Karati D, Molecular docking and pharmacokinetic evaluations of curcumin-based scaffolds as MDM2-p53 inhibitors. *Discov Chem*, 2 (2025) 1.
27 Kurmi SPC, Thapa S, Mahmood AAR, Murav AK, Biradar MS, Bhagyanath N & Chauhan S, Medicinal chemistry insights of molecular docking and cell permeability mechanism of phytoconstituents present in Mimosa pudica as NS2B-NS3 protease inhibitors against dengue virus. *Discov Chem*, 2 (2025) 78.
28 Thapa S, Biradar MS, Nargund SL, Ahmad I, Agrawal M, Patel H & Rane V, Synthesis, molecular docking, molecular dynamic simulation studies, and antitubercular activity evaluation of substituted benzimidazole derivatives. *Adv Pharmacol Pharm Sci*, 2024 (2024) 1.
29 Prasad S, Thapa S, Metri SM & Suresha M, Molecular docking, drug-likeness properties, and toxicity prediction of alkaloidal phytoconstituents of Piper longum against monoamine oxidase enzyme-A as an anti-depressive agent. *Discov Chem*, 2 (2025) 1.
30 Jawarkar RD, Sharma P, Jain N, Gandhi A, Mukerjee N, Al-Mutairi AA & Shastri MD, QSAR, molecular docking, MD simulation and MMGBSA calculations approaches to recognize concealed pharmacophoric features requisite for the optimization of ALK tyrosine kinase inhibitors as anticancer leads. *Molecules*, 27 (2022) 1.
31 Pattar SV, Adhoni SA, Kamanavalli CM & Kumbar SS, *In silico* molecular docking studies and MM/GBSA analysis of coumarin-carbonodithioate hybrid derivatives divulge the anticancer potential against breast cancer. *Beni-Suef Univ J Basic Appl Sci*, 9 (2020) 1.
32 Gritsenko OV, Koopmans' theorem and its density-functional-theory analog assessed in evaluation of the red shift of vertical ionization potential upon complexation. *Chem Phys Lett*, 691 (2018) 178.
33 Kalarani R, Sankarganesh M, Kumar GGV & Kalanithi M, Synthesis, spectral, DFT calculation, sensor, antimicrobial and DNA binding studies of Co (II), Cu (II) and Zn (II) metal complexes with 2-amino benzimidazole Schiff base. *J Mol Struct*, 1206 (2020) 127725.
34 Sandeep W, Omkar D, Harshada M, Aaditi P, Prajwal G, Deepak G & Anil S, Evaluation of phytochemical & antimitotic potential of Annona reticulata extracts by onion root model. The 24th International Electronic Conference on Synthetic Organic Chemistry, (2020) 137.
35 Chester K, Zahiruddin S, Ahmad A, Khan W, Paliwal S & Ahmad S, Bioautography-based identification of antioxidant metabolites of Solanum nigrum L. and exploration of its hepatoprotective potential. *Pharmacogn Mag*, 13 (2017) 179.
36 Yasmin R, Gogoi S, Bora J, Chakraborty A, Dey S, Ghaziri G & Rahman M, Novel insight into the cellular and molecular signalling pathways on cancer preventing effects of Hibiscus sabdariffa: a review. *J Cancer Prev*, 28 (2023) 77.
37 Pucci C, Martinelli C & Ciofani G, Innovative approaches for cancer treatment: current perspectives and new challenges. *Ecancermedicalscience*, 13 (2019) 1.
38 Black LE, Longo JF & Carroll SL, Mechanisms of receptor tyrosine-protein kinase ErbB-3 (ERBB3) action in human neoplasia. *Am J Pathol*, 189 (2019) 1898.
39 Tomuleasa C, Tigu AB, Munteanu R, Moldovan CS, Kegyes D, Onaciu A &Irimie A, Therapeutic advances of targeting receptor tyrosine kinases in cancer. *Signal Transduct Target Ther*, 9 (2024) 1.
40 Singh G, Rohit, Kumar P & Aran KR, Targeting EGFR and PI3K/mTOR pathways in glioblastoma: innovative therapeutic approaches. *Med Oncol*, 42 (2025) 97.
41 Lu L, Zhuang Z, Fan M, Liu B, Yang Y, Huang J & Zhao L, Green formulation of Ag nanoparticles by *Hibiscus rosa-sinensis*: introducing a novel chemotherapeutic drug for the treatment of liver cancer. *Arab J Chem*, 15 (2022) 1.
42 Petry S, Mechanisms of mitotic spindle assembly. *Annu Rev Biochem*, 85 (2016) 659.
43 Mihajlović AI, Haverfield J & Fitz Harris G, Distinct classes of lagging chromosome underpin age-related oocyte aneuploidy in mouse. *Dev Cell*, 56 (2021) 2273.